Fischer, T., Hainzl, S. (2017): Effective Stress Drop of Earthquake Clusters. - *Bulletin of the Seismological Society of America*, *107*, 5, pp. 2247—2257.

DOI: http://doi.org/10.1785/0120170035

THE SEISMOLOGICAL SOCIETY OF AMERICA
400 Evelyn Ave., Suite 201
Albany, CA 94706-1375
(510) 525-5474; FAX (510) 525-7204
www.seismosoc.org

Bulletin of the Seismological Society of America, Vol. 107, No. 5, pp. 2247–2257, October 2017, doi: 10.1785/0120170035

Effective Stress Drop of Earthquake Clusters

by Tomáš Fischer and Sebastian Hainzl

Abstract The static stress drop is a standard measure of the average decrease of shear stress on a fault during an earthquake. It has been observed that stress drop does not vary significantly with earthquake magnitude and may be regarded as an invariant parameter of the rupture process at different scales. Although typical stress drops of earthquakes range between 1 and 10 MPa, much smaller stress drops in fractions of MPa are reported for slow earthquakes and in some cases also for earthquake swarms. For the latter cases, the effective stress drop was introduced as an alternative parameter that makes use of the cumulative seismic moment and total activated area of the seismic cluster. In this article, we test how the effective stress drop is comparable to the static stress drop of a single earthquake rupturing the same fault portion. To this purpose, we compare the spatiotemporal evolution of the seismic moment release and analyze the uncertainties of the estimated stress drops. We show that the effective stress drop is only comparable to earthquake stress drops in specific cases. In particular, the effective stress-drop values significantly underestimate the earthquake stress drops in the presence of aseismic deformation. The values are only scale independent if prestress and poststress conditions are uniform in space. Our analysis of data from injection-induced seismicity, natural earthquake swarms, and aftershock sequences shows that in most cases the effective stress-drop estimate is rather stable during the cluster evolution. However, slightly increasing estimates for injection-induced seismicity are indicative for the local forcing of the system. Although the effective stress drops of natural and induced seismicity in geothermal projects range from 0.1 to 3 MPa, those related to fracking in hydrocarbon formations are anomalous low, from 0.08 to 1.8 kPa, which hints to the important role of aseismic deformations.

Introduction

Static stress drop is a fundamental measure of stress released during an earthquake. Its value scales with the seismic moment of the earthquake and is inversely related to the third power of the characteristic rupture dimension, which introduces large errors in its estimates. Estimations for individual events show a large scatter, with typical values between 0.1 and 100 MPa. In contrast, the average value is found to be almost independent of the rupture size over several orders of magnitudes, indicating a self-similar rupture process (Kanamori and Anderson, 1975; Kwiatek *et al.*, 2011; Michálek and Fischer, 2013). Some recent results indicate that stress drops of swarms and slow earthquakes are only on the order of fractions of MPa and thus relatively small (e.g., Brodsky and Mori, 2007; Chen and Shearer, 2011). However, some of these studies are based on a different approach to estimate the stress drop. Instead of determining the stress drop of single earthquakes, they use the relation between the size of the activated area and the cumulative seismic moment of the sequence (Roland and McGuire, 2009). Whereas the uncertainty of spectral-based static stress-drop estimations results from the uncertainty of seismic moment and corner frequency (Cotton *et al.*, 2013), the stress drop estimated from earthquake clusters depends on the uncertainty of seismic moment, the location accuracy, and catalog completeness.

Our study deals with the second type of stress drop, which we denote effective stress drop and is measured by comparing the cumulative seismic moment and areal extent of a seismic cluster. It, thus, differs from the traditional static stress drop, which refers to a single event and is usually determined using the low-frequency asymptote of the ground-displacement spectrum. A similar quantity has been examined by several authors, though only some of them use the term effective stress drop. To our knowledge, the first one was our analysis of the 2000 seismic swarm in West Bohemia (Hainzl and Fischer, 2002), which showed that the cumulative seismic moment scaled during the swarm evolution with the third power of the radius of convex area enclosing hypocenter locations projected to a plane. Vidale and Shearer (2006) found that some clusters in southern California show large spatial extent compared to their cumulative moment. Chen *et al.* (2012) determined the final effective stress drop of these bursts in the 3–8 MPa range. Roland and McGuire (2009)

found that effective stress drop of swarms in southern California and the Galapagos ridge ranges from 0.04 to 4.3 MPa.

In this article, we examine the concept of effective stress drop in terms of uncertainties and their origin in data. We analyze the evolution of the scaling between the seismic moment and the size of the event cluster with respect to different types of seismic activity and fault rheology. Finally, we apply our approach to various types of injection-induced and natural seismicity to determine their effective stress drops and unveil the characteristics of these sequences.

Stress Release on the Fault

In the following, we discuss the relation between the stress drop and the seismic moment release for simple end-member models of a single rupture (model A) and a series of events (models B–D) relaxing the static stress in a given fault patch.

Rupturing by a Single Event (Model A)

First, we consider a circular fault segment of radius r with uniform prestress that is fully unloaded by one slip event (model A). In this case, the scalar seismic moment M_0 is proportional to r^3, and the corresponding slip is proportional to $\sqrt{1-x^2/r^2}$, in which x is the distance to the center (Brune, 1970; Madariaga and Ruiz, 2016). This corresponds to a single seismic event, which breaks the whole segment and leads to a constant stress drop within the rupture area. The static stress drop represents the difference $\Delta\tau$ between the shear stress directly before and after the slip event. The stress drop of a circular crack is related to the seismic moment M_0 according to

$$\Delta\tau_{\text{eff}} = \frac{7}{16}\frac{M_0}{r^3} \tag{1}$$

(see, e.g., review of Madariaga and Ruiz, 2016).

Let us now consider the case in which stress is uniformly relaxed by a series of earthquakes instead of one single event, with the same static stress drop in the end. If numerous smaller ruptures release the accumulated stress stepwise, different scenarios may occur, depending on the rheology of the fault and density of asperities, which influences the stress interactions among individual events. In general, we can differentiate between three slip scenarios: (1) slip only occurs seismically (brittle rheology), (2) slip is partly released aseismically and partly seismically (mixed rheology), or (3) all slip occurs aseismically (ductile rheology). In the following, we discuss the first two cases, which are related to earthquake occurrences, with regard to the dependence of the effective stress drop $\Delta\tau_{\text{eff}}$ on the observed cumulative seismic moment release ΣM_0 and the size R of the activated fault region (R is used to distinguish cumulative area of ruptures from a single rupture). According to the stress drop of a single crack (equation 1), the effective stress drop is determined in this case by

$$\Delta\tau_{\text{eff}} = \frac{7}{16}\frac{\sum M_0}{R^3}. \tag{2}$$

Model B: Compact Asperities

In the case of a brittle fault rheology, the piecewise rupturing of the fault segment by numerous small earthquakes requires some mechanism preventing the simultaneous rupturing of the whole segment. Possible reasons might be, for example, the presence of barriers, inhomogeneous loading, or dilatancy due to pore creation (Yamashita, 1999; Aki and Richards, 2002). For our purpose, we do not need to specify the specific process. We only assume that the circular brittle fault segment consists of densely distributed asperities that can rupture individually (model B in Fig. 1). Because of their closeness, elastic stress transfer between the asperities is important. If a constant slip direction is assumed, due to the regional stress field, slip on one asperity always increases the shear stress in its surrounding. This leads to stress concentrations in front of the rupture zone, enhancing the failure of adjacent asperities. However, it also reloads recently ruptured asperities that are weak due to persisting small dynamic friction. The frictional strength is significantly reduced after a rupture and recovers with the logarithm of time (Rabinowicz, 1958; Scholz, 1998). Hence, re-rupturing of these asperities is promoted. In this way, the asperities in the fault segment can be sequentially unloaded and reloaded. In an ideal case, this process continues until the stress is fully released within the whole fault segment. As a result, the event number is the highest in the central part of the fault segment, so that the total slip predicted by the crack solution for the same circular fault area (model A) is accommodated. Because of the rerupturing of asperities, the summed area of individual ruptures exceeds the area of the fault segment. This implies a cubic scaling of the seismic moment with the radius R of the ruptured fault segment, similar to the case of instantaneous rupturing by a single seismic event. Provided that the stepwise rupturing totally releases the stress, the effective stress drop is close to the static stress drop of an equivalent single large rupture.

Models C and D: Asperities Embedded in a Ductile Environment

Many faults are, however, not fully brittle and are known to consist of a spatially inhomogeneous rheology with varying brittle (velocity weakening) and ductile (velocity strengthening) properties. Observational evidence stems from inhomogeneous coupling coefficients, fault creep, and repeating earthquakes (Lay and Kanamori, 1981; Miyazaki *et al.*, 2004; Harris, 2017). Numerical simulations of brittle asperities embedded in a ductile environment show that the asperities on such fault segments might rupture either simultaneously as a single earthquake or separately as individual events, depending on the distance between the asperities and the frictional strength of the ductile region. For a high density

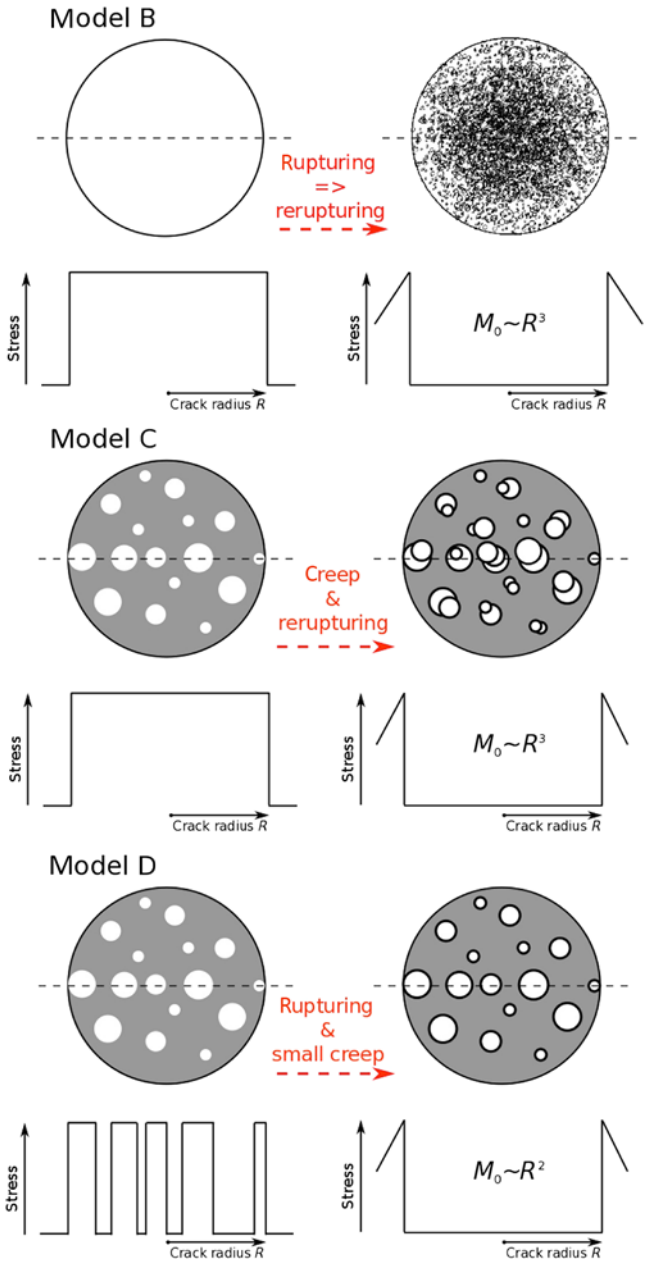

Figure 1. Characteristics of the rupture surface, stress state, and rupture process for three different synoptic models; (left column) initial state and (right column) final state. The dashed line in the upper plots indicate the cross section used for the stress values in the lower plots. Brittle asperities are indicated by white circles, and the ductile rupture surface is gray; the black edge indicates asperities that have slipped. Model B shows brittle rupture with uniform prestress, which is released by rupturing and rerupturing due to stress transfer and reloading. Model C shows ductile rupture with sporadic brittle asperities and uniform prestress, which is released by simultaneous rupturing and creep. Both of these processes reload the rupture and lead to rerupturing. In model D, the stress is nonuniform because ductile parts were unloaded by previous creep. Rupturing of brittle asperities alone is not sufficient to reload the rupture, which results in the absence of rerupturing. The color version of this figure is available only in the electronic edition.

of the asperities and/or a small $a - b$ frictional parameter in the ductile region, simultaneous rupturing of the asperities occurs (Kaneko *et al.*, 2010; Dublanchet *et al.*, 2013; Yabe and Ide, 2017). Although we are not dealing with this case in our study, it is interesting to note that the coseismic stress drop is heterogeneous in this case, and spectral estimations based on the crack model are known to underestimate the local stress drop of the asperities (Madariaga, 1979). However, here, we are concerned with the case that those asperities rupture separately, leading to an observed sequence of clustered seismicity.

In this case of a mixed rheology with brittle asperities sparsely distributed within a ductile environment, the relevance of aseismic creep for stress transfer depends on the initial stress condition on the fault segment at the time of the rupture initiation. Models C and D in Figure 1 represent two end members of this behavior with the same maximum of the prestress level. In model C, the prestress is constant along the whole rupture area at zero time, for example, due to an external loading of the fault segment. In this case, the simultaneous action of aseismic creep and seismic events reloads the asperities, and the creeping parts foster the repeated rupturing of the same brittle compartments (Guglielmi *et al.*, 2015). In particular, the creep leads locally to a stress reduction but increases the stress at adjacent asperities, resulting in repeated rupturing of the asperities. Heavy overlap between subsequent seismic events occurs. Similar to model B, this complies with the cubic scaling of the total seismic moment with the radius R of the fault segment, if the density of asperities is uniform in space. However, although individual events release the total stress in their locations, the effective stress drop is strongly underestimated in this case, because a large portion of stress is released aseismically.

In contrast, in the other end-member case (model D), the prestress is assumed to be zero in ductile parts, due to precursory creep. In this case, failure of an asperity induces only minor creep in its vicinity. Because of the relatively large distances between adjacent asperities, neither the elastic stress transfer nor the induced creep sufficiently reloads previously ruptured neighboring asperities. As a result, asperities are not repeatedly ruptured, and subsequent earthquakes do not overlap. Accordingly, the total seismic moment is expected to simply scale with the area, that is, the square of the radius R of the ruptured fault segment, in the case of a uniform density of the asperities. This leads to a scale-dependent bias of stress-drop estimations manifested in the decrease of the effective stress drop with the spatial size R according to $1/R$ (see equation 2). This case is related to the analysis of Tumarkin *et al.* (1994) who found that the seismic moment scaling of a composite source of uniformly distributed crack sources is not equivalent to that of a single crack. Similar to model C, the effective stress drop is strongly underestimated, due to (precursory) aseismic unloading. A similar behavior might be expected for aftershocks occurring on asperities within the mainshock rupture in which the prestress has been released in between by the mainshock rupture.

To summarize, the above analysis shows that, in the case of brittle and mixed rheology with homogeneous prestress (models B and C), the total slip amount is characterized by a cubic scaling of seismic moment with earthquake cluster radius $\Sigma M_0 \sim R^3$, whereas in the case of a partly ductile fault with heterogeneous prestress (model D), the seismic moment only scales with the square of the radius $\Sigma M_0 \sim R^2$. However, the effective stress drop only equals the static stress drop in model B, whereas it is expected to be much lower than the true static stress drop in cases represented by models C and D.

Application to Seismic Clusters

We tested the concept of effective stress drop on selected seismic data of various types (Table 1), including seven data sets of injection-induced seismicity, two data sets of earthquake swarms, two mainshock–aftershock sequences, and one case of a creeping fault. The references to the corresponding publications and the basic characteristics of these sequences, such as magnitude range, total seismic moment, total duration, hypocenter depths, and error estimates, are provided in Table 1. If the scalar seismic moment or moment magnitude was not provided, we converted local magnitudes to seismic moments using the empirical formula $\log M_0 = 1.1\, M_L + 10.09$ (H. Jakoubková, personal comm., 2017), which was derived for the local magnitude scale used by the West Bohemia Seismic Network. Even smaller scaling of 1.0 between $\log M_0$ and M_L was found, for example, by Rognvaldsson and Slunga (1994) for the seismicity in Iceland. The small scaling factor between $\log M_0$ and M_L agrees with the proportionality factor of 1.5 between M_L and M_w for small earthquakes (Deichmann, 2017). In the cases when the total seismic moment was provided along with the M_L magnitudes, the seismic moments of individual events were scaled accordingly (indicated in Table 1 by asterisks). The larger uncertainty of deriving seismic moments from local magnitudes is reflected in the larger error estimate (see the Methods section).

The used data represent areal extent corresponding to the radius of the convex area ranging from less than 50 m to 30 km. Microseismic activity induced by hydraulic fracturing has the smallest areal extent of the seismicity cluster ($R < 100$ m). This case is represented by four data sets: (1) the earthquake catalog related to hydraulic fracturing in tight gas sands in Cotton Valley (Texas), which consists of 272 events with location error less than 2 m (Rutledge and Phillips, 2003); (2, 3) the Canyon Sands (Texas) data set, which includes 3500 and 5400 locations of events triggered during injection stages 2 and 3, with the mean location errors of 11 m (Fischer *et al.*, 2008); and (4) the Woodford shale gas data set (Oklahoma) involving 814 events with location errors below 50 m (Anikiev *et al.*, 2014).

Earthquake clusters of medium areal extent ($R < 2$ km) are represented by induced seismicity during hydraulic stimulation of geothermal reservoirs and by earthquake swarms. We used data sets from Soultz-sous-Forêts with 7200 events during the 2000 injection in the GPK-2 borehole, 4700 events during the 2003 injection in the GPK-3 borehole (Dorbath *et al.*, 2009), and the Basel 2006 injection, including 1980 events with location precision better than 15 m (Kraft and Deichmann, 2014). Earthquake swarm seismicity includes earthquake swarms of 2000 and 2011 and mainshock–aftershock sequence of 2014 in West Bohemia/Vogtland, all with location errors smaller than 100 m (Fischer *et al.*, 2014; Hainzl *et al.*, 2016). For the largest areal extent ($R \sim 50$ km), we used the precise relocations of the Sierra el Mayor aftershock sequence of the M_w 7.2 mainshock in southern California in 2010 (Hauksson *et al.*, 2012). Effective stress drop of creeping faults is analyzed using the double-difference relocated catalog of the Parkfield section of the San Andreas fault (SAF) between longitudes −121.6° and −120.4° (Northern California Earthquake Data Center [NCEDC], 2014), with a single M_w 5.1 earthquake and five $M_w > 4.5$ earthquakes in the period from 1990 to 2016. For the Sierra el Mayor sequence, the reported relative location errors were 3 m; no location errors were available for the Parkfield data set. Because of similar character of these data (the same location methodology and large areal extent), we used the same conservative location error estimate of 100 m for both data sets.

Methods

Prior to measuring the activated fault area, outliers have been removed by requiring that each event should have at least five neighbors within a specified distance range, which is chosen according to the size of the hypocenter cloud (0.1 km for hydraulic-fracture-induced events, 0.5 km for geothermal-induced events and earthquake swarms, and 10 km for the plate-boundary faults).

Then, the activated area was measured after projecting the hypocenters to the main plane, which was determined by singular-value decomposition. For the projected locations, the radius R of the activated area was calculated using the convex envelope algorithm (convhull) implemented in MATLAB, which determines the smallest area A that contains the hypocenter projections within a convex hull. The radius is then simply determined by $R = \sqrt{A}/\pi$. To examine the temporal evolution of the ruptured area, we determine R for the first N events with $N \in \langle 4, L \rangle$, in which L is the total number of events in the sequence, and 4 is the minimum size of the event cluster required by the convex hull algorithm. The same window was used to determine the total seismic moment ΣM_0 and the estimate of the corresponding effective stress drop $\Delta\tau_{\mathrm{eff}}$ using equation (2).

According to Cotton *et al.* (2013), we assume that the size of the rupture (radius R of the convex area in our case), seismic moment, and stress drop have lognormal distributions. Then, by applying the error propagation law to equation (1), one gets

$$\sigma^2_{\log \Delta\tau} = \sigma^2_{\log M_0} + 9\sigma^2_{\log R}, \tag{3}$$

Table 1
Analyzed Data Sets of Natural and Induced Seismicity

Data Set	Reference	Number of Events	Magnitude	ΣM_0 (N·m)	Depth (km)	R_{max} (km)	Duration	Migration Speed	Aspect Ratio	$\Delta\tau_{eff}$ (kPa)
				$\log_{10}$ Error		Error (km)				$\log_{10}$ Error
Cotton Valley, stage 3	Rutledge and Phillips (2003)	272	Not provided	2.0×10^{8}*	2.7	0.036	4 hrs	9 m/hr	12	1.8
				0.70		**0.002**				**0.72**
Canyon Sands, stage 2	Fischer *et al.* (2008)	3830	M_w	3.1×10^{8}*	1.6	0.046	1.5 hrs	30 m/hr	10	1.4
			−2.8 to −1.4	**0.70**		**0.011**				**0.75**
Canyon Sands, stage 3	*Fischer et al. (2008)*	*5820*	M_w	2.3×10^{8}*	*1.6*	*0.052*	*2 hrs*	*26 m/hr*	*10*	*0.73*
			−3.0 to −1.2	***0.70***		***0.011***				***0.71***
Woodford Shale	*Anikiev et al. (2014)*	*814*	M_w	1.9×10^{10}	*1.8*	*0.48*	*2.8 days*	*7 m/hr*	*1.8*	*0.08*
			−2.5 to 1.6	***0.70***		***0.05***				***0.76***
Soultz 2000	Dorbath *et al.* (2009)	5049	M_L	1.7×10^{14}*	4.5	0.6	10.5 days	4.7 m/hr	2.3	340
			−1.0 to 2.5	**0.30**		**0.039**				**0.31**
Soultz 2003	*Dorbath et al. (2009)*	*4728*	M_L	1.5×10^{14}*	*4.5*	*0.78*	*46 days*	*0.7 m/hr*	*1.8*	*140*
			−0.5 to 2.9	***0.30***		***0.085***				***0.33***
Basel 2006	*Kraft and Deichmann (2014)*)	*1980*	M_w	2.5×10^{14}	*4.5*	*0.33*	*12 months*	*0.9 m/day*	*4.4*	*3000*
			0–2.9	***0.3***		***0.015***				***0.31***
West Bohemia 2008 swarm	Fischer *et al.* (2014)	3900	M_L	1.1×10^{15}	6–10	1.3	111 days	0.5 m/hr	7.6	230
			0–3.5	**0.48**		**0.03**				**0.49**
West Bohemia 2011 swarm	*Fischer et al. (2014)*	*9500*	M_L	2.5×10^{15}	*6–10*	*1.2*	*32 days*	1.5 m/hr	*4.5*	*810*
			0–3.6	***0.48***		**0.040**				***0.48***
West Bohemia 2014 M 4.3 MAF	*Hainzl et al. (2016)*	*2800*	M_L	1.5×10^{15}	*6–9*	*0.84*	*103 days*	*0.3 m/hr*	*5*	*1100*
			0–4.3	***0.48***		***0.075***				***0.49***
Sierra El Mayor 2010 M 7.2 MAF	*Hauksson et al. (2012)*	*6200*	M_w	8.1×10^{19}	*3–20*	*25*	*67 days*	*n/a*	*6.1*	*2300*
			2.0–7.2	***0.30***		***0.100***				***0.30***
Parkfield creep section, −121.6° to −120.4°, 1990–2016	*NCEDC (2014)*	*5940*	M_D	6.7×10^{16}	*3–12*	*16*	*27 yrs*	*n/a*	*16*	*70*
			1.6–5.0	***0.48***		***0.100***				***0.48***

The data shown in Figures 2 and 3 are indicated in italics. The total moment ΣM_0 marked by asterisks was provided by the author of the data; otherwise it was calculated in this study. The migration speed is estimated by the ratio between the maximum size of the cluster R_{max} and the duration; $\Delta\tau_{eff}$ stands for the effective stress drop. MAF, mainshock–aftershock sequence. Bold values indicate error.

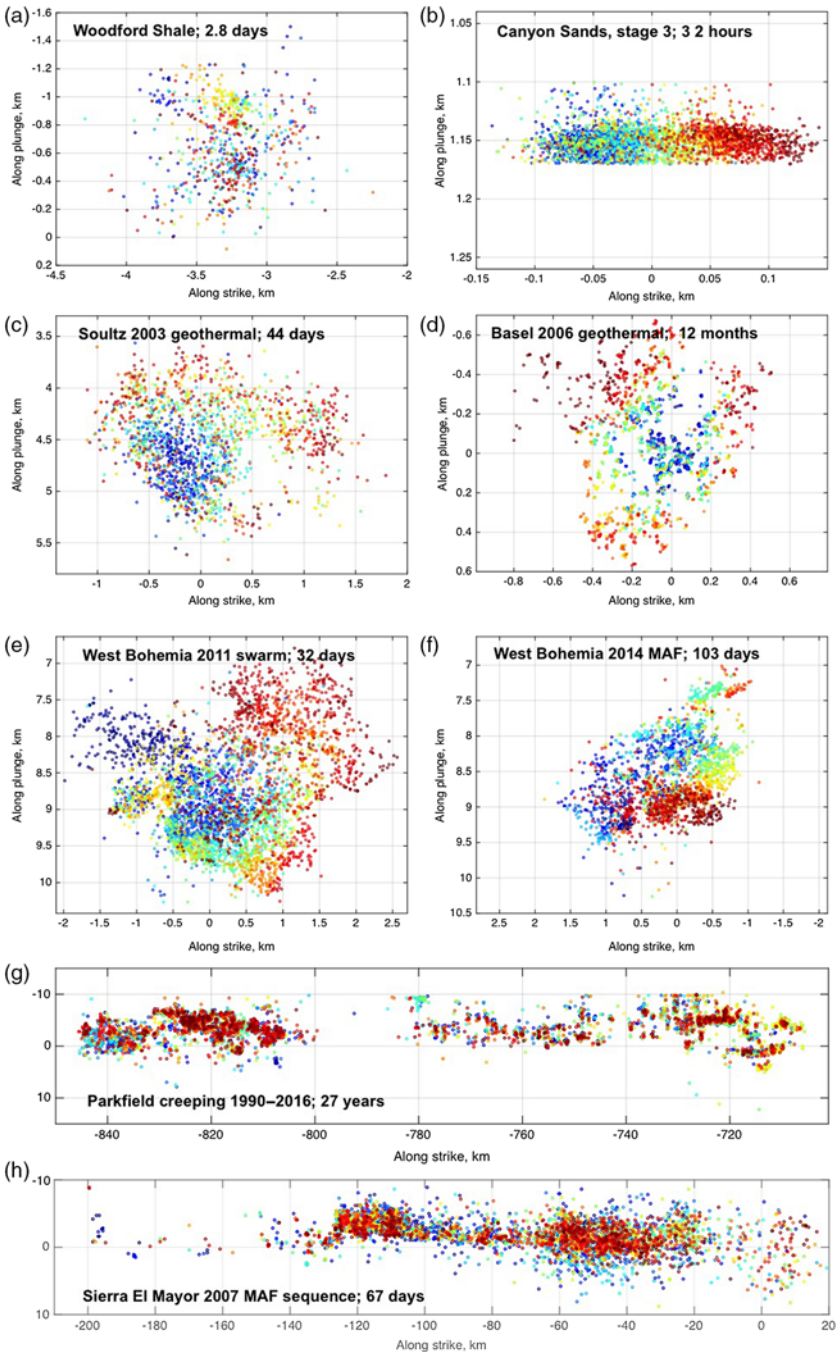

Figure 2. Hypocenter distribution of selected seismic sequences; gray scale (color from blue to red in online version) indicates the sequence order of individual events. (a–d) Injection-induced seismicity and (e) earthquake swarm. (f, h) Mainshock–aftershock sequences (MAF) and (g) creeping fault. The durations of analyzed sequences range from 2 hrs to 27 yrs and are indicated within each plot. The color version of this figure is available only in the electronic edition.

which shows the prevailing effect of location errors compared to errors in seismic moment. We estimate the logarithmic error of seismic moment $\sigma_{\log M_0}$ as 0.3 for M_0 determined from M_w, 0.5 for M_0 determined from M_L and M_D, and 0.7 for hydraulic-fracture-induced seismicity, for which the seismic moment is expected to be the most uncertain. The total seismic moment is also affected by the completeness magnitude of the earthquake catalog. According to Zakharova *et al.* (2013), the ratio between the total seismic moment release and the observed one for events in the magnitude range $[M_c, M_{max}]$:

$$C = \frac{M_0^{tot}}{M_0^{obs}} = (1 - 10^{-(1.5-b)(M_{max}-M_c)})^{-1}. \quad (4)$$

It turns out that for $b < 1.4$, the ratio C is smaller than 2.0 for the magnitude range of 3 that is fulfilled by our data. Regarding the fact that the b-value of the analyzed data sets is around 1.0, we consider the effect of the incomplete catalog negligible, compared to the uncertainty of the seismic moment estimate itself.

The uncertainty σ_R of the cluster size is estimated as the convex size R of the first events (five selected as optimal), which are expected to be collocated in the cases of swarms and injection-induced seismicity, where the seismic events migrate from a single origin. For events at the SAF, we use 100 m as the location uncertainty estimate. Then, σ_R is converted to the relative logarithmic uncertainty as $\sigma_{\log R} = \log(1 + \sigma_R/R)$.

Results

Table 1 shows the results of the effective stress-drop analysis along with the basic characteristics of the sequences. These are the maximum radius R_{max} of the convex hull, aspect ratio of the cloud, and effective stress drop. The aspect ratio is measured as the average standard deviation of in-plane coordinates normalized by the standard deviation of the off-plane coordinates. It is expected to increase with increasing planarity of the hypocenter cloud. The highest aspect ratios above 10 are obtained for hydraulic fracturing of sands and the Parkfield section of SAF and the lowest value of 1.8 for shale gas fracking and the Soultz-sous-Forêts injection in 2003. For eight different seismic sequences, Figure 2 shows the in-plane coordinates of the seismicity with color-coded sequential ordering. For the same cases, Figure 3 shows the result for the evolution of the cumulative seismic moment release ΣM_0, as well as the estimated effective stress drop $\Delta\tau_{eff}$ as a function of the cluster radius R. These plots reveal various patterns, which are discussed below.

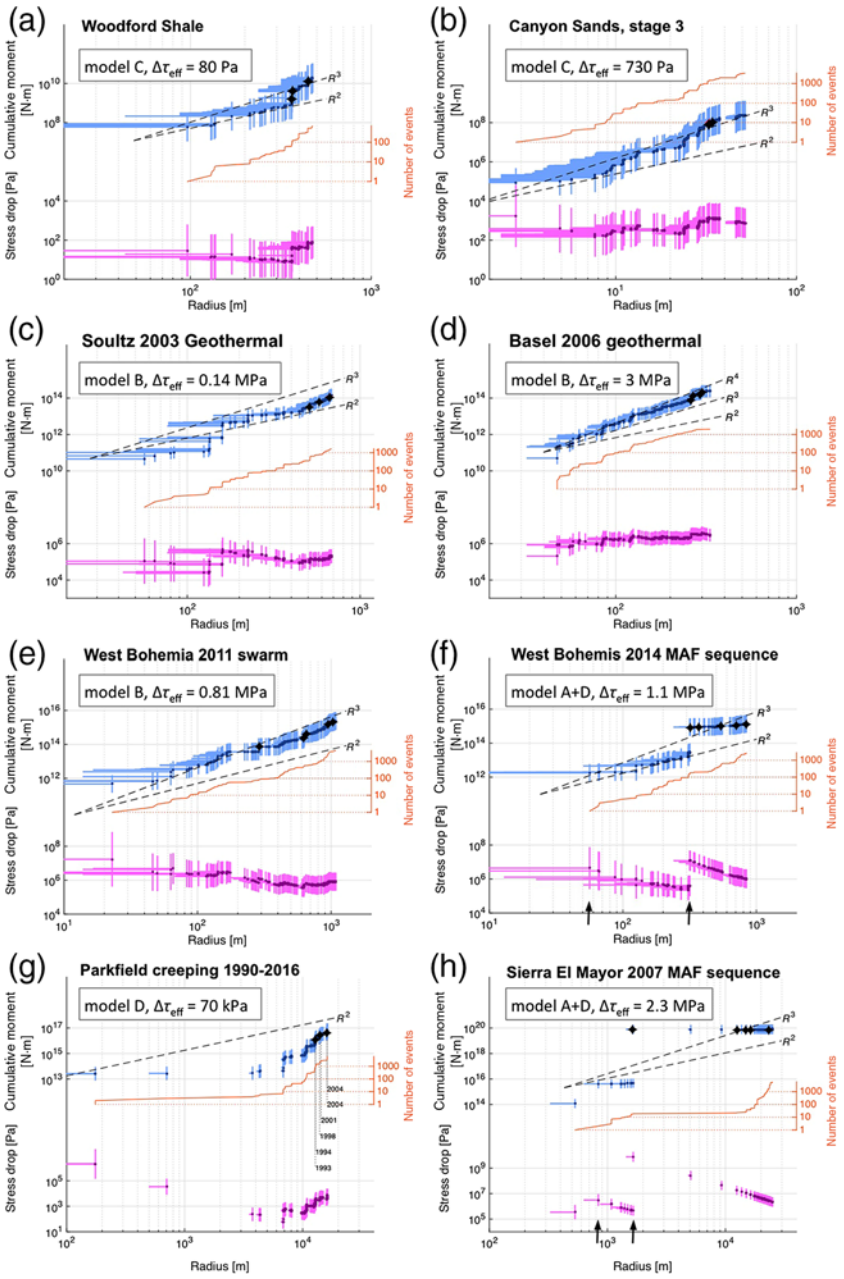

Figure 3. Evolution plots of total seismic moment ΣM_0, cumulative number of events and effective stress drop $\Delta\tau_{\text{eff}}$ of selected seismic sequences with hypocenters shown in Figure 2. The black diamonds in the seismic moment plot indicate the five strongest events in each sequence. In each panel, the most suitable rupture model and final effective stress drop are indicated. The error bars indicate the logarithmic uncertainties of analyzed quantities following equation (2). For the radius R, only the left-pointing error bars are shown, expressing the fact that the location error overestimates the true area activated by seismic activity. In (f) and (h), vertical arrows indicate the time of mainshocks, and in (g) the vertical lines with year labels indicate $M > 4.5$ earthquakes. The color version of this figure is available only in the electronic edition.

Scaling of $\Sigma M_0(R)$

The injection-induced seismicity (Fig. 3a–d) is characterized by an overall stable estimation of the effective stress drop, which corresponds to an approximate increase of the total seismic moment with the third power of the earthquake cluster radius R. However, the mean value of the stress-drop estimate increases a bit during the evolution of some of these sequences. In some cases (a. Woodford Shale, b. Canyon Sands, and c. Soultz-sous-Forêts, 2003), the seismic moment growth is only episodic, which is probably related to activation of asperities in the stimulated volume. In cases (b) and (c), a slow growth of seismic moment with spreading of the area occurs in the initial phase of activity, which likely results from the relative large location errors of these data sets. Because of location errors, R is strongly overestimated (and thus the effective stress drop underestimated) in the initial phase in which the location error of single events is comparable to the cluster extension. This holds for all the sequences, except the plate margin seismicity (Fig. 3g,h), for which the cluster size of kilometers exceeds the estimated location errors significantly. A relatively stable effective stress-drop estimation is observed for Basel geothermal injection and for the West Bohemia earthquake swarm of 2011 (Fig. 3d,e), with almost a steady-state increase of ΣM_0. The scaling of ΣM_0 exceeds R^3 for Basel and approaches R^3 for the 2011 swarm, which is consistent with the R^3 scaling of the West Bohemia earthquake swarm of 2000 found by Hainzl and Fischer (2002).

In contrast, the mainshock–aftershock sequences in West Bohemia and California (Fig. 3f,h) display an abrupt increase of total seismic moment during the mainshock followed by a slow or even negligible increase during the aftershock activity, in which the effective stress drop decreases steadily to its final value. However, the initial and final values lie approximately on the R^3 scaling line. The creeping part of the SAF north of Parkfield (Fig. 3g) shows a fast increase of the radius R of the activated area, with only a small increase of cumulative seismic moment, which results in a weak scaling of ΣM_0 with R, for which the exponent is only about 1. In fact, the only significant contributions to ΣM_0 are the $M > 4.5$ earthquakes, for which the origin dates are indicated by vertical lines.

Effective Stress Drop $\Delta\tau_{\mathrm{eff}}$

The effective stress drops of the processed seismic sequences range over 4.5 orders from 80 Pa to 3 MPa (Table 1 and Figs. 3 and 4). The smallest $\Delta\tau_{\mathrm{eff}}$ in the range from 80 Pa to 1.8 kPa are observed for seismicity accompanying hydraulic fracturing of gas-bearing shales and sands, which points to a dominating aseismic deformation in place. This is in accordance with the rupture model C, in which creep plays a significant role in reloading of ruptures. Hydraulic stimulations of geothermal reservoirs and seismic swarms are associated by significantly larger effective stress drops from 0.14 to 3.0 MPa, which is at the lower margin of static stress drops of natural seismicity. Along with the cubic power-law scaling, this corresponds to the rupture model B, in which the fractures are reloaded seismically. Effective stress drops of mainshock–aftershock sequences exceed 1 MPa, which approaches the static stress drops of mainshocks. The mainshock itself represents a single rupture, for which model A holds; aftershocks occur in the area where most of the stress has been released by the mainshock, so reloading is not sufficient for rerupturing, and model D is in place. The aftershocks, if they are sufficiently numerous but not large, mainly highlight the mainshock slip area but do not significantly contribute to the cumulative seismic moment release. As a result, the final effective stress-drop estimate is close to the static stress drop of the mainshock. Anomalous low effective stress drops are observed for the creeping section of the SAF; the cumulative value for 27 yrs is 70 kPa, which is equivalent to an annual rate of only 3 kPa. This is, however, not unexpected in the Parkfield area, where aseismic creep is considered the main mechanism responsible for releasing the accumulated strain (Johanson and Burgmann, 2005; Rolandone *et al.*, 2008).

Discussion

As shown in the previous sections, the final value of the effective stress drop is close to the static stress drop of an equivalent single rupture (model A) of the same size in the case in which no aseismic loading takes place and asperities are reruptured during the sequence, so that the sum of their area scales with the third power of the radius of the activated fault patch (model B). If aseismic loading occurs or rerupturing is weak, the effective stress drop is smaller than the static stress drop (model C). This is probably the case of tight sands and shale gas fracking in Figure 3a,b, in which aseismic loading is expected. On the other hand, the effective stress drop can exceed the static stress drop in the case of solely seismic loading and long-term injection, resulting in repeated activation of fault patches, which could be the case of the Basel geothermal data set (Fig. 3d).

Uncertainty of $\Delta\tau_{\mathrm{eff}}$

According to Figure 3, the logarithmic uncertainty of effective stress-drop estimates is quite similar to the logarithmic uncertainty of seismic moment, which was estimated as 0.3, 0.5, and 0.7 for data sets of a different type. This holds namely for the larger radii R, because the uncertainty of effective stress drop decreases with increasing R. This results from the fact that the uncertainty of R is derived from the location error, which does not depend on the size of the cluster R. On the contrary, for the total seismic moment, its logarithmic uncertainty is constant, which results in the dominance of errors in seismic moment compared to errors in locations. Accordingly, the larger weight of location errors in equation (2) is suppressed by a much higher logarithmic uncertainty of seismic moments. Here, we find a different situation than in the case of static stress-drop estimates, in which the radius R converts to the corner frequency f_c, for which the logarithmic uncertainty is constant. Thus, in the case of static stress drops, which are estimated in the frequency domain, the influence of errors in f_c dominates (Cotton *et al.*, 2013). This is in contrast to the effective stress drops, for which the influence of errors in seismic moment is the largest. The relatively small effect of location errors for estimating the effective stress drops, however, presumes that location outliers are removed prior to the analysis. This can be easily checked by the $\Sigma M_0(R)$ evolution plot, for which the large location errors are pronounced by a fast growth of R compared to ΣM_0 that is also expressed by a small exponent of the ΣM_0 scaling (see Fig. 3).

$\Sigma M_0(R)$ Evolution

Besides the final value of the effective stress drop defined by the total seismic moment release and the final cluster extension, the analysis of the evolution of the seismic moment release with cluster size provides some additional insights. Especially, an increase which significantly diverges from R^3 scaling can be indicative of specific situations. In the Stress Release on the Fault section, we explained that the range of scaling exponents from 2 (model D) to 3 (models B and C) is conditioned by a uniform asperity density in space and no ongoing local aseismic loading during the cluster evolution. However, smaller or larger exponents are possible, if these assumptions are not valid. In particular, smaller exponents might, for example, occur in model D, if the density of asperities or the prestress decreases with distance from the initiation point of the sequence. In contrast, exponents larger than 3 can be expected if stress is continuously reloaded by an aseismic source in the central part of the cluster, which might lead to re-rupturing in the central part without significant extension of the cluster size. Here, we remind the reader that the exponent of $\Sigma M_0(R)$ scaling exceeds 3 for the injection-induced seismicity. This can be explained by massive fluid injection that decreases the effective normal stress and also increases differential stress by poroelastic coupling (Segall and Lu, 2015). This is observed namely during the Basel geothermal injection (Fig. 3d) and also the Canyon Sands gas fracking (Fig. 3b), in which the massive reruptur-

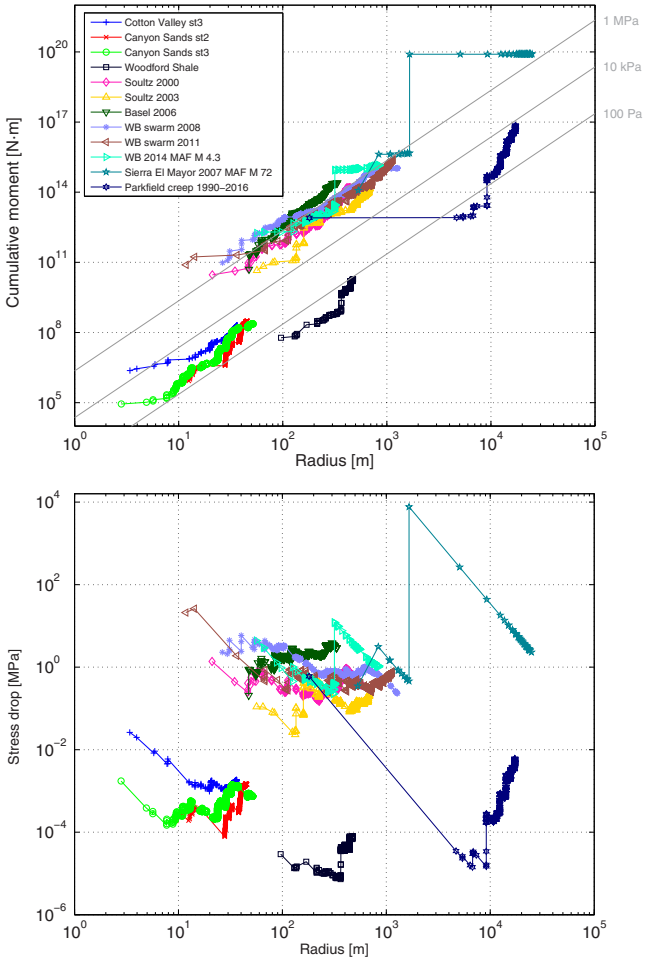

Figure 4. (Top) Cumulative seismic moment and (bottom) effective stress drop of all analyzed sequences. Error bars are not shown for the sake of clarity; WB, West Bohemia. The color version of this figure is available only in the electronic edition.

ing occurs at extremely low-effective stress-drop levels of hundreds of pascals.

Altogether, very small effective stress drops (up to dozens of kPa) occur during hydraulic fracking of shales and sands and also at the Parkfield creeping section of SAF. This could be interpreted by two scenarios: (1) a small shear modulus or (2) a large portion of creep in the total slip. For Parkfield, the second scenario holds, based on the comparison of the large geodetic slip rate up to 20 mm/yr (e.g., Roeloffs, 2001) and the small seismic moment release. Direct measurements of fault slip and seismic activity induced by fluid injection into a natural fault (Guglielmi *et al.* 2015) show that fluid injection triggers primarily aseismic slip, and microearthquakes are induced as a secondary effect; the total seismic moment was by more than two orders of magnitude smaller than the total released moment. The same relation would apply to the ratio of effective and static stress drops in this experiment, which would clarify the effective stress-drop deficit in the case of hydraulic fracturing observed in our study. Indeed, with regard to the fact that the rigidity of sands and shales is of the same order as the rigidity of other types of rocks, it appears probable that, during hydraulic fracturing of these gas-bearing formations, a high portion of strain is released aseismically, and seismic radiation represents only a small part.

Other Relations

It is important to note that in cases with scaling different from R^3, the estimation of the effective stress drop depends on the cluster size. Consequently, the estimation becomes size and time dependent, because the cluster size increases with time. In particular, if the scaling is smaller than 3, $\Delta\tau_{\mathrm{eff}}$ decreases with the increasing size of the cluster, as observed namely for the initial period of some sequences (see Fig. 4). Thus, the effective stress-drop value should be evaluated for the complete seismic sequences. A scaling exponent smaller than 3 could be also related to 1D seismicity spreading, which may occur in some cases of dike intrusions and similar geometries.

Another important point to note is that the estimation of the effective stress drop depends on the cumulative properties and not explicitly on time. Although time information would provide additional information, it would also complicate the analysis. The modeling of the timing would require additional assumptions of the particular triggering mechanism and a more complex approach. For example, the employment of rate- and state-dependent friction laws to describe the spatiotemporal seismicity rate as a function of the stressing history would require at least three additional model parameters, as well as the calculation of the stress changes due to earthquake–earthquake interaction and aseismic loading (Dieterich, 1994). Furthermore, local heterogeneity further increases the complexity of real time series. Our approach has the advantage that it ignores the complex interevent times and focuses only on the spatial growth as a function of the event number in relation to the cumulative seismic moment release.

Conclusions

Stress drop is an important parameter for ground-motion prediction as well as for understanding the seismogenic process. Although suspect of large uncertainties, the stress-drop estimation of single earthquakes is well established, based on either spectral analysis or inverted coseismic slip distributions. Similar to the latter, the concept of the effective stress drop of a seismic sequence is based on the cumulative seismic slip, which is estimated from the cumulative seismic moment. Assuming a uniform stress release within the spatial seismicity cluster, the crack solution is used to calculate the effective stress drop from the activated area and cumulative seismic moment. However, we show that the estimated value is only in agreement with the stress drop of a single event rupturing the same area (model A) if no aseismic deformation takes place and rerupturing of asperities occurs

during the sequence (model B). In all other cases, the measured effective stress drop does not represent the static stress drop in this fault portion, particularly because aseismic deformation releases stress in a part of the fault. Furthermore, the evolution of the cumulative seismic moment release as a function of the cluster radius can be used to discriminate different processes. A uniformly loaded fault region with a uniform density of asperities is expected to lead to stable scale-independent effective stress-drop estimates. In contrast, the effective stress-drop estimation becomes scale dependent if ongoing external local loading or a fractal spatial distribution of asperities leads respectively to higher or lower exponents than 3.

Our analysis of 12 sequences ranging from injection-induced activity to natural-swarm and aftershock activity shows some common and different characteristics. Three seismicity groups can be distinguished: a low-stress-drop group of shale and gas fracking; a normal-stress-drop group of geothermal injections, swarms, and mainshock–aftershock sequences; and the very low-stress-drop case of creeping events. After neglecting the initial slow increase of ΣM_0 of some sequences that occurred most likely due to a large location error, the standard cubic scaling of the total seismic moment is found. Slightly higher exponents in the case of injection-induced sequences are indicative of the ongoing local forcing related to the massive fluid injections during the cluster evolution, whereas lower exponents down to 1 in the case of creeping events might be related to a decreasing/fractal asperity density.

Data and Resources

Catalog data used in this study are available by contacting the corresponding author. The data analysis and plotting was carried out in MATLAB, https://www.mathworks.com/products/matlab.html (last accessed May 2017).

Acknowledgments

Metadata for this study were accessed through the Northern California Earthquake Data Center (NCEDC), doi: 10.7932/NCEDC, and the West Bohemia Seismic Network, doi: 10.7914/SN/WB. The authors are grateful to reviewers Christine J. Ruhl and Piero Poli, and Associate Editor Cezar I. Trifu for their valuable comments that helped improve the article. The work of T. F. was supported by the Czech Science Foundation (Grant Number 16-10116J) and by the Ministry of Education, Youth and Sports (Grant Number LM2015084).

References

Aki, K., and P. G. Richards (2002). *Quantitative Seismology*, Second Ed., University Science Books, Sausalito, California, 574.

Anikiev, D., J. Valenta, F. Stanek, and L. Eisner (2014). Joint location and source mechanism inversion of microseismic events: Benchmarking on seismicity induced by hydraulic fracturing, *Geophys. J. Int.* **198,** 249–258, doi: 10.1093/gji/ggu126.

Brodsky, E. E., and J. Mori (2007). Creep events slip less than ordinary earthquakes, *Geophys. Res. Lett.* **34,** L16309, doi: 10.1029/2007GL030917.

Brune, J. N. (1970). Tectonic stress and the spectra of shear waves from earthquakes, *J. Geophys. Res.* **75,** 4997–5009.

Chen, X., and P. M. Shearer (2011). Comprehensive analysis of earthquake source spectra and swarms in the Salton Trough, California, *J. Geophys. Res.* **116,** no. B09309, doi: 10.1029/2011JB008263.

Chen, X., P. M. Shearer, and R. E. Abercrombie (2012). Spatial migration of earthquakes within seismic clusters in Southern California: Evidence for fluid diffusion, *J. Geophys. Res.* **117,** no. B04301, doi: 10.1029/2011JB008973.

Cotton, F., R. Archuleta, and M. Causse (2013). What is sigma of the stress drop? *Seismol. Res. Lett.* **84,** 42–48, doi: 10.1785/0220120087.

Deichmann, N. (2017). Theoretical basis for the observed break in $M_L = M_w$ scaling between small and large earthquakes, *Bull. Seismol. Soc. Am.* **107,** doi: 10.1785/0120160318.

Dieterich, J. (1994). A constitutive law for rate of earthquake production and its application to earthquake clustering, *J. Geophys. Res.* **99,** no. B2, 2601–2618, doi: 10.1029/93JB02581.

Dorbath, L., N. Cuenot, A. Genter, and M. Frogneux (2009). Seismic response of the fractured and faulted granite of Soultz-sous-Forêts (France) to 5 km deep massive water injections, *Geophys. J. Int.* **177,** 653–675, doi: 10.1111/j.1365-246X.2009.04030.x.

Dublanchet, P., P. Bernard, and P. Favreau (2013). Interactions and triggering in a 3-D rate-and-state asperity model, *J. Geophys. Res.* **118,** 2225–2245, doi: 10.1002/jgrb.50187.

Fischer, T., S. Hainzl, L. Eisner, S. Shapiro, and J. Le Calvez (2008). Microseismic signatures of hydraulic fracture growth in sediment formations: Observations and modeling, *J. Geophys. Res.* **113,** no. B02307, doi: 10.1029/2007JB005070.

Fischer, T., J. Horálek, P. Hrubcová, V. Vavryčuk, K. Bräuer, and H. Kämpf (2014). Intra-continental earthquake swarms in West-Bohemia and Vogtland: A review, *Tectonophysics* **611,** 1–27, doi: 10.1016/j.tecto.2013.11.001.

Guglielmi, Y., F. Cappa, J.-P. Avouac, P. Henry, and D. Elsworth (2015). Seismicity triggered by fluid injection-induced aseismic slip, *Science* **348,** 1224–1226, doi: 10.1126/science.aab0476.

Hainzl, S., and T. Fischer (2002). Indications for a successively triggered rupture growth underlying the 2000 earthquake swarm in Vogtland/NW-Bohemia, *J. Geophys. Res.* **107,** no. B12, 2338, doi: 10.1029/2002JB001865.

Hainzl, S., T. Fischer, H. Čermáková, M. Bachura, and J. Vlček (2016). Aftershocks triggered by fluid-intrusion: Evidence for the aftershock sequence occurred 2014 in West Bohemia/Vogtland, *J. Geophys. Res.* **121,** 2575–2590, doi: 10.1002/2015JB012582.

Harris, R. A. (2017). Large earthquakes and creeping faults, *Rev. Geophys.* **55,** 169–198, doi: 10.1002/2016RG000539.

Hauksson, E., W. Yang, and P. M. Shearer (2012). Waveform relocated earthquake catalog for southern California (1981 to 2011), *Bull. Seismol. Soc. Am.* **102,** no. 5, 2239–2244, doi: 10.1785/0120120010.

Johanson, I. A., and R. Burgmann (2005). Creep and quakes on the northern transition zone of the San Andreas fault from GPS and InSAR data, *Geophys. Res. Lett.* **32,** L14306, doi: 10.1029/2005GL023150.

Kanamori, H., and D. L. Anderson (1975). Theoretical basis of some empirical relations in seismology, *Bull. Seismol. Soc. Am.* **65,** 1073–1095.

Kaneko, Y., J.-P. Avouac, and N. Lapusta (2010). Towards inferring earthquake patterns from geodetic observations of interseismic coupling, *Nature Geosci.* **3,** 363–369, doi: 10.1038/NGEO843.

Kraft, T., and N. Deichmann (2014). High-precision relocation and focal mechanism of the injection-induced seismicity at the Basel EGS, *Geothermics* **52,** 59–73.

Kwiatek, G., K. Plenkers, and G. Dresen (2011). Source parameters of picoseismicity recorded at Mponeng deep gold mine, South Africa: Implications for scaling relations, *Bull. Seismol. Soc. Am.* **101,** no. 6, 2592–2608, doi: 10.1785/0120110094.

Lay, T., and H. Kanamori (1981). An asperity model of large earthquake sequences, in *Earthquake Prediction: An International Review*, D. W. Simpson and P. G. Richards (Editors), American Geophysical Union, Washington D.C., 579–592.

Madariaga, R. (1979). On the relation between seismic moment and stress drop in the presence of stress and strength heterogeneity, *J. Geophys. Res.* **84,** no. B5, 2243–2250.

Madariaga, R., and S. Ruiz (2016). Earthquake dynamics on circular faults: A review 1970–2015, *J. Seismol.* **20,** 1235–1252, doi: 10.1007/s10950-016-9590-8.

Michálek, J., and T. Fischer (2013). Source parameters of the swarm earthquakes in West Bohemia/Vogtland, *Geophys. J. Int.* **195,** 1196–1210, doi: 10.1093/gji/ggt286.

Miyazaki, S., P. Segall, J. Fukuda, and T. Kato (2004). Space time distribution of afterslip following the 2003 Tokachi-oki earthquake: Implications for variations in fault zone frictional properties, *Geophys. Res. Lett.* **31,** L06623, doi: 10.1029/2003GL019410.

Northern California Earthquake Data Center (NCEDC) (2014). *Northern California Earthquake Data Center. UC Berkeley Seismological Laboratory. Dataset*, doi: 10.7932/NCEDC.

Rabinowicz, E. (1958). The intrinsic variables affecting the stick-slip process, *Proc. Phys. Soc.* **71,** 668–675.

Roeloffs, R. (2001). Creep rate changes at Parkfield, California 1966–1999: Seasonal, precipitation induced, and tectonic, *J. Geophys. Res* **106,** 16,525–16,547, doi: 10.1029/2001JB000352.

Rognvaldsson, S. T., and R. Slunga (1994). Single and joint fault plane solutions for microearthquakes in south Iceland, *Tectonophysics* **237,** 73–80.

Roland, E., and J. J. McGuire (2009). Earthquake swarms on transform faults, *Geophys. J. Int.* **178,** 1677–1690, doi: 10.1111/j.1365-246X.2009.04214.x.

Rolandone, F., R. Burgmann, D. C. Agnew, I. A. Johanson, D. C. Templeton, M. A. d'Alessio, S. J. Titus, C. DeMets, and B. Tikoff (2008). Aseismic slip and fault-normal strain along the central creeping section of the San Andreas fault, *Geophys. Res. Lett.* **35,** L14305, doi: 10.1029/2008GL034437.

Rutledge, J. T., and W. S. Phillips (2003). Hydraulic stimulation of natural fractures as revealed by induced microearthquakes, Carthage Cotton Valley gas field, east Texas, *Geophysics* **68,** 441–452.

Segall, P., and S. Lu (2015). Injection-induced seismicity: Poroelastic and earthquake nucleation effects, *J. Geophys. Res.* **120,** 5082–5103, doi: 10.1002/2015JB012060.

Scholz, C. H. (1998). Earthquakes and friction laws, *Nature* **391,** 37–42.

Tumarkin, A. G., R. J. Archuleta, and R. Madariaga (1994). Scaling relations for composite earthquake models, *Bull. Seismol. Soc. Am.* **84,** 1279–1283.

Vidale, J. E., and P. M. Shearer (2006). A survey of 71 earthquake bursts across southern California: Exploring the role of pore fluid pressure fluctuations and aseismic slip as drivers, *J. Geophys. Res.* **111,** no. B05312, doi: 10.1029/2005JB004034.

Yabe, S., and S. Ide (2017). Slip-behavior transitions of a heterogeneous linear fault, *J. Geophys. Res.* **122,** 387–410, doi: 10.1002/2016JB013132.

Yamashita, T. (1999). Pore creation due to fault slip in a fluid-permeated fault zone and its effect on seismicity: Mechanism of earthquake swarm, *Pure Appl. Geophys.* **155,** 625–647.

Zakharova, O., S. Hainzl, and C. Bach (2013). Seismic moment ratio of aftershocks with respect to main shocks, *J. Geophys. Res.* **118,** 5856–5864, doi: 10.1002/2013JB010191.

Faculty of Science
Charles University
Albertov 6
12843 Prague, Czech Republic
fischer@natur.cuni.cz
(T.F.)

GFZ German Centre for Geosciences
Helmholtzstraße 6/7
14467 Potsdam, Germany
(S.H.)

Manuscript received 2 February 2017;
Published Online 25 September 2017